Check for updates

Early detection of bacteria using SPR imaging and event counting: experiments with *Listeria monocytogenes* and *Listeria innocua*†

Marine Boulade, [ID]ab Alexandra Morlay,ac Felix Piat,c Yoann Roupioz,a
Thierry Livache,ad Paul G. Charette,b Michael Canvab and Loïc Leroy*a

Foodborne pathogens are of significant concern in the agrifood industry and the development of associated rapid detection and identification methods are of major importance. This paper describes the novel use of resolution-optimized prism-based surface plasmon resonance imaging (RO-SPRI) and data processing for the detection of the foodborne pathogens *Listeria monocytogenes* and *Listeria innocua*. With an imaging spatial resolution on the order of individual bacteria (2.7 ± 0.5 µm $\times$ 7.9 ± 0.6 µm) over a field of view 1.5 mm^2, the RO-SPRI system enabled accurate counting of individual bacteria on the sensor surface. Using this system, we demonstrate the detection of two species of *Listeria* at an initial concentration of 2×10^2 CFU mL^{-1} in less than 7 hours. The surface density of bacteria at the point of positive detection was 15 ± 4 bacteria per mm^2. Our approach offers great potential for the development of fast specific detection systems based on affinity monitoring.

1 Introduction

Rapid microbial detection and identification is of great concern for consumer safety, in particular in the agri-food industry where perishable goods must be screened for pathogen contamination.[1–3] Listeriosis for example, a bacterial infection by *Listeria monocytogenes*, one of the main foodborne pathogens, causes a variety of severe illnesses with fatality rates as high as 30%.[4] However, all current testing methods for these bacteria require an incubation period lasting from 24 h to several days.[5] As a result, significant work in academia and industry has focused on the development of rapid and affordable pathogen detection tools[6,7] such as dedicated biosensors.[8,9]

Various types of surface-based biosensors have proven effective for the detection of pathogens such as surface acoustic wave (SAW) sensors,[10] impedance sensors,[11–13] the quartz crystal microbalance (QCM),[14,15] and surface plasmon resonance (SPR).[16,17] Such sensors are compact, versatile, respond in real time, can be fabricated at low cost, and do not require molecular labeling.[18] Using modern microfabrication methods, these sensors can be configured in a matrix layout, thus enabling

parallel detection to screen for multiple species or concentrations simultaneously. With SPR, the entire sensor surface can be imaged (termed "SPRI"), with the surface partitioned into arbitrary sized "spots" with location-specific surface functionalization for parallel detection applications.[19]

In the case of biosensors that rely on surface detection, improvement in performance rely on three main strategies: improving the probability of contact of the target molecules with the sensing surface (efficacy and dynamics of mass transport towards the surface), increasing the efficiency of the surface probes (specificity and efficacy of capture of the targets), and enhancing the sensitivity of the transducer to improve the lower limit of detection. The first strategy is used, for instance, in biosensors that employ microfluidic mixing,[20,21] electrophoresis[22] or immunoseparation.[23] The second strategy has spawned much research in optimizing the nature of the probes[24] and immobilization strategies.[25–28] In the third strategy, efforts have focused on increasing the performance of the transducer,[29] labelling the targets with non-intrusive secondary molecules,[30] and on chemically amplifying the response.[31]

SPRI systems are easily automated and compatible with real food samples.[9,19,32,33] Optical coupling can be achieved with gratings,[34] microscope objectives[35,36] or prisms,[19,32,37,38] with prism-based SPRI being the most frequently used configuration for the detection of bacteria. Prism-based SPRI systems are often designed with a relatively wide field of view (around 1 cm^2) for parallel measurements on a matrix of spots (spotted microarray) with detection levels as low as 100 pM in the case of DNA–DNA hybridization.[38,39] Though prism-based SPRI systems

aINAC-SyMMES, Univ. Grenoble Alpes, CEA, CNRS, 38000 Grenoble, France. E-mail: loic.leroy@univ-grenoble-alpes.fr

bLaboratoire Nanotechnologies Nanosystèmes (LN2), CNRS UMI-3463, Université de Sherbrooke, UGA, 3000 Boulevard Université, J1K 0A5, Québec, Canada

cPrestodiag, 1 Mail du Professeur Georges Mathé, F-94800 Villejuif, France

dAryballe Technologies, 17 Avenue des Martyrs, 38000 Grenoble, France

are limited in spatial resolution to tens of microns or more by geometrical aberrations caused by the prism,[40] this is not a problem for spotted microarray applications since the spots are sufficiently large (100 microns in diameter or more) and spatially well separated. In true imaging applications of biological objects such as bacteria, however, where the morphology and/or dynamical behaviour of individual objects is the basis for the information sought, the low spatial resolution results in loss of important information.

In this article, we propose a new strategy to improve the performance of bacterial detection using resolution optimized (RO) surface plasmon resonance imaging (RO-SPRI). The strategy is based on extending the high spatial resolution of SPRI, typically restricted to a narrow band in the middle of the image and falling off towards the edges, to the entire field of view, thereby significantly improving the accuracy of the surface kinetics analysis.[40] We demonstrate faster positive signature identification based on single bacteria observation compared to SPRI analysis based on aggregate spots responses. Our observations are confirmed with standard differential interference coherence (DIC) microscopy.[41] To our knowledge, this is the first time that SPRI is used for bacterial detection based on counting and trajectory analysis of individual bacteria.

2 Experimental section

2.1 Microbiology culture

Two *Listeria* species were used in this study: *Listeria monocytogenes* and *Listeria innocua* from naturally contaminated food products provided by the Institut Scientifique d'Hygiène et d'Analyse (ISHA, Massy, France). The bacterial species, from stock suspension conserved at −80 °C, were streaked on Tryptone-Soy Agar (TSA, Biomérieux, France) plates and incubated overnight at 37 ± 1 °C. Prior to experiments, one colony of the strain of interest was inoculated in 10 mL of Tryptic Soy Broth (TSB, Sigma-Aldrich, Missouri, USA) at 37 ± 1 °C, 150 rpm for 18 h ± 2 h. The bacterial concentration was then adjusted to 1 ± 0.2 MacFarland (McF) with a densitometer (Biomérieux, France) by adding Buffer Peptone Water (BPW, Biomérieux, France).

For each experiment, six serial dilutions (1 : 10) were carried out with TSB. 200 μL of one of the six dilutions corresponding to the targeted concentration was injected into the RO-SPRI fluidic chamber and processed on the biochips. Other samples of 200 μL were also done in parallel and kept at the same temperature as the experimental chamber (37 °C). The bacterial concentration was then controlled every hour for four hours (plus initial time) by spreading 100 μL of the sixth dilution on two TSA plates. The colony counting was performed after overnight incubation at 37 ± 1 °C.

2.2 Biochip preparation

N-SF66 glass prisms with an apex angle of 83° and a width of 12 mm (ref. 40) (Schott, Switzerland) formed the base of the RO-SPRI biochips. Thin films of 2 nm of chromium and 53 nm of gold were deposited on the prism base (the sensor surface) by

evaporation. The prism bases were then plasma cleaned (40 W, 0.6 mbar, 75% oxygen, 25% argon) for 3 minutes (Femto 300, Diener Electronic, Germany) to prepare the surface for chemical functionalization.

Three antibodies provided by Prestodiag (Villejuif, France) were used for surface spot functionalization: two polyclonal antibodies (LiM14 and LiM16) specific to *Listeria monocytogenes* and one polyclonal antibody (Lis12) specific to *Listeria innocua*. One monoclonal antibody (KLH), directed against Keyhole Limpet Hemocyanin (obtained from L. Bellanger CEA Marcoule, France), *i.e.* not directed against bacterial targets, was used as a negative control in all experiments.

The biochip surface functionalization was prepared with an electro-polymerization process described in detail elsewhere.[19,42] Electropolymerization of the solution (1 μM of antibodies coupled with NHS-pyrrole, 10 μM of free NHS-pyrroles in spotting buffer) was carried out using a Microgrid spotter (BioRobotics). Biochips were then washed with phosphate buffer solution (PBS) and final surface passivation was performed using 1% (w/v) bovine serum albumin (Sigma Aldrich, Saint Quentin Fallavier, France) for 15 min at room temperature, ensuring very low non-specific binding.[43] The biochips were washed again with PBS and kept in PBS at 4 °C for up to several weeks.[44,45]

Before being introduced into the RO-SPRI system, described in detail the next section, the non-coated faces of the prism were thoroughly washed and cleaned to avoid any optical defects.

2.3 Apparatus set-up

The set-up was designed to demonstrate and validate the use of resolution-optimized prism-based SPRI (RO-SPRI) for bacterial detection. The system was coupled to a differential interference contrast (DIC) microscope for simultaneous observation during the experiments.

Resolution-optimized prism-based SPR imaging (RO-SPRI) system. The RO-SPRI system used in the experiments is depicted in Fig. 1 and is described in detail elsewhere.[40] The light source consists of a high-power LED M735F1 (Thorlabs, New
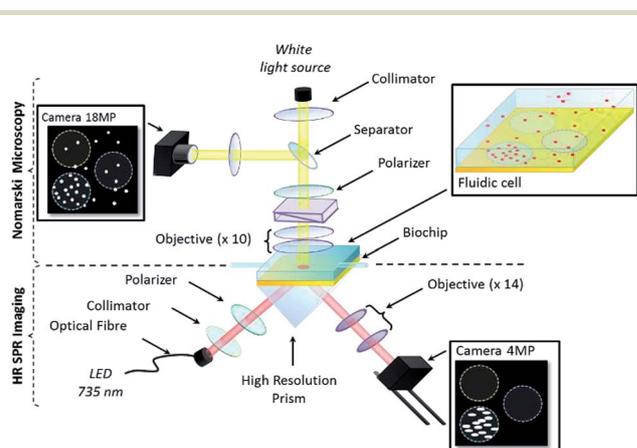

Fig. 1 Dual DIC microscopy and RO-SPR imaging apparatus.

Jersey, USA), of centre wavelength 735 nm, coupled to an optical fiber (1 mm diameter core), collimated by a 35 mm focal length aspheric achromatic lens. The resulting beam is then selected for transverse-magnetic or transverse-electric polarization using a rotating linear polarizer before entering the prism. Light reflected at the prism/fluid interface is imaged by a CMOS sensor (ORCA 4.0, Hamamatsu, 2048 × 2048 resolution, 16 bits per pixel) using a custom-made 14× objective consisting of 210 mm and 15 mm focal lengths convex lenses.

Note that in prism-based SPRI, the image plane usually is not perpendicular to the optical axis of the system, *i.e.* there is a skew between the camera image plane and the sensor surface, resulting in only a narrow band being in focus at any time in the image, with resolution dropping off towards the edges due to progressive loss of focus.[40] The amount of skew is dependent on the geometry of the prism and dictates the width of the "in-focus" band at the centre of the image. In RO-SPRI, a 15 images sequence is captured corresponding to a series of focal plane step-changes designed to scan the "in-focus" band across the image. The images in the sequence are then processed to combine them into a single "RO-SPRI image" that is in focus across the entire image thereby having uniform spatial resolution. In the experiments described below, one RO-SPRI image was generated every 3 minutes.

Note also that due to the propagative nature of the surface plasmons, the spatial resolution in the direction parallel to plasmon propagation is ultimately limited by the propagation length of the surface plasmons.[46] In our case, spatial resolution in the direction parallel to plasmon propagation is ~6 μm. Even if better resolution can be reached using other settings, these choices appeared to be a satisfactory compromise between spatial and temporal resolution for the targeted application.

Differential interference coherence (DIC) microscopy system. DIC images were recorded simultaneously with a color 18 MP CMOS sensor (Canon 600D) mounted on an upright Olympus microscope (U-MDIC, Olympus, Japan), with a 10× objective (MPFLN10X Olympus), placed above the SPRI set-up (Fig. 1). The RO-SPRI system and the DIC microscope were set to record the same area on the biochip and both cameras were synchronized for simultaneous acquisition.
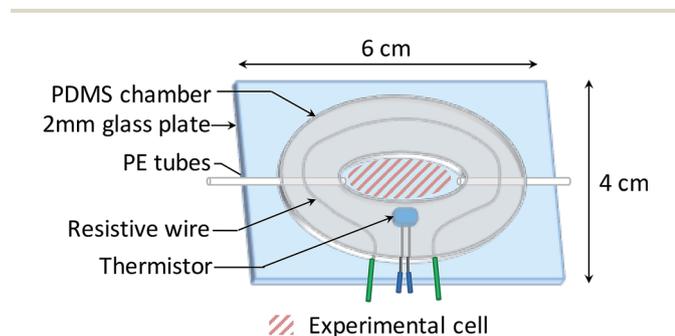

Fig. 2 Schematic diagram of the fluidic chamber.

2.4 Fluidic chamber

The bacterial suspensions were injected on the biochip surface through a custom-made temperature regulated fluidic chamber, enabling bacterial growth during experiments. As shown in Fig. 2, a 200 μL fluidic chamber was fabricated from a 1.5 mm thick PDMS film and then glued to a 2 mm thick glass plate after plasma activation (40 W, 0.6 mbar, 75% O₂, 25% Ar for 30 s, Femto 300, Diener Electronic, Germany). Fluids were injected through 600 μm diameter PE tubes.

The temperature regulation was carried out by a heating circuit made of resistive wires contouring the chamber, supplied with a variable voltage. The voltage was regulated using a PID controller tuned by the measurement of the temperature through a thermistor. The variability of the temperature was ±0.15 °C, which is adequate for microbiology applications.[47] Note that SPR signal variations induced by a 0.15 °C temperature variation (about 0.02% reflectivity) are much smaller than the SPR reflectivity changes that indicate the presence of bacteria on the sensor surface (>1% reflectivity).[48,49] The operating temperature for the experiments was set at 37 °C.

2.5 Data processing

Image processing. Reference RO-SPRI and DIC images at the beginning of each experiment were stored and subtracted from all following images to remove inhomogeneity due imperfections on the biochip surface and static intensity variations between the chemically different areas. The resulting images are named "differential RO-SPRI images" and "differential DIC images" below.

Event counting. The number and location of high-intensity features or "events" indicating the presence of bacteria in the RO-SPRI images were calculated using the ImageJ (http://imagej.nih.gov/ij/) Fiji "Trackmate" plugin (https://fiji.sc/).[50] The filters used for object detection were Laplacians of a Gaussian (LoG) with a dimensions of 7.4 μm and 2 μm for the RO-SPRI images and DIC images, respectively, as determined experimentally from the data. The spatial distribution of high-intensity features (events) indicating the presence of individual bacteria within each antibody-functionalized spot were calculated using Matlab, with an average surface density of bacteria determined per each spot.

SPRI sensorgrams. For comparison with conventional prism-based SPRI, an aggregate analysis per spot area was also performed on the RO-SPRI images. The same spots as in the event counting analysis were used and kinetic curves were calculated by computing the mean differential intensity averaged over each spot. This kind of analysis will be referred to as "SPRI sensorgrams" as often found in the literature.[51–55]

3 Results and discussion

In the experiments, several concentrations of *L. monocytogenes* and *L. innocua* were injected into the fluidic chamber and RO-SPRI and DIC images were acquired over time using the dual imaging apparatus.
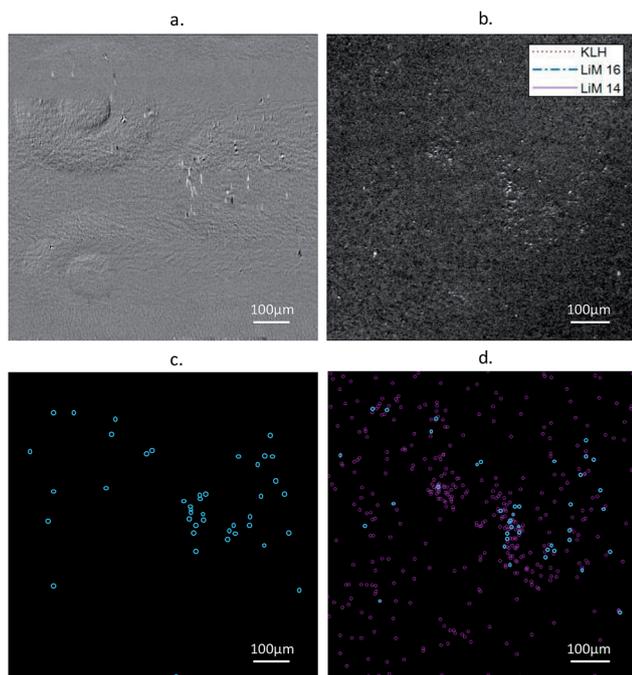
Fig. 3 Results from an experiment with an injection of *L. monocytogenes* at 2×10^2 CFU mL^{-1}, images were taken 400 min after injection. (a) Differential RO-SPRI image (b) differential microscopy (DIC) image, (c) and (d) results of the event detection using ImageJ on (a) and (b), respectively – events detected both in the RO-SPRI and DIC images are colored in blue.

3.1 Image comparison between RO-SPRI images and DIC microscopy images

A comparison of images and event detection, carried out on both types of images, is presented Fig. 3. The images correspond to an experiment with an original concentration of *L. monocytogenes* at 2×10^2 CFU mL^{-1}, starting at 400 min after injection into the fluidic chamber.

Under these conditions, high-intensity events indicating the presence of individual bacteria in the RO-SPRI micrographs (Fig. 3a) were 2.7 ± 0.5 μm $\times$ 7.9 ± 0.6 μm in size on average along the directions perpendicular and parallel to plasmon propagation, respectively. *L. monocytogenes* is a bacterium of average size 2 μm $\times$ 0.5 μm $\times$ 0.5 μm, the discrepancy along one of the two planar dimensions being due to loss of spatial resolution associated with plasmon propagation. In the DIC microscopy images, the bacteria have an estimated size of 2.0 ± 0.2 μm $\times$ 0.7 ± 0.2 μm, the variability being due both to the variability in the actual size of the bacteria and to the low magnification of the objective which was fixed at $10\times$ to obtain a field of view compatible with the RO-SPRI system.

The event counting data processing (Fig. 3c and d) showed that more particles were detected in the DIC images. This is due to the difference in the depth of field between the two methods: the evanescent field associated with the surface plasmons has a penetration depth in the dielectric of less than 300 nm at a wavelength of 740 nm, while the DIC microscope has a depth of field of around 8 μm for the $10\times$ objective. As the images were taken while the bacterial solution was still in the chamber,
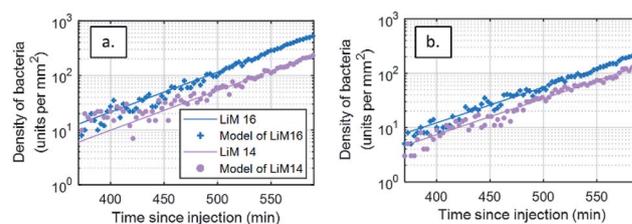

Fig. 4 Modelling of *Listeria monocytogenes* bacterial growth from event-detection data in both types of images from areas functionalized with antibodies targeting *L. monocytogenes* (LiM16 and LiM14). Number of bacteria respectively detected on images (a) DIC and (b) RO-SPRI images on both specific antibody areas and their model fits – injection at 10^2 CFU mL^{-1}.

bacteria in the volume could be observed in the DIC images outside the penetration depth of the SPRI system, explaining the difference in the number of bacteria observed with each imaging system. For larger densities of bacteria, the difference could also be related to the lower spatial resolution of the RO-SPRI system causing close events to merge and not to be discernible. This is of minor concern for early diagnostics, *i.e.* for low concentration detection, provided there is no factor promoting aggregation.

3.2 Quality control of the bacterial growth conditions in the fluidic chamber

The biocompatibility of the fluidic chamber was validated by assessing the doubling time of *L. monocytogenes* during experiments from the DIC microscopy images. As the depth of field of this method is of several microns, the number of bacteria detected over time is a direct assessment of growth in the solution. In the absence of flow, the evolution of the number of bacteria, $N(t)$, in DIC microscope images on a surface S, depends solely on diffusion and gravity and can be calculated with: $N(t) = C_0 \exp(t/\tau) \times S \times v \times t$, where v is the sedimentation speed and τ the growth rate of the bacteria.

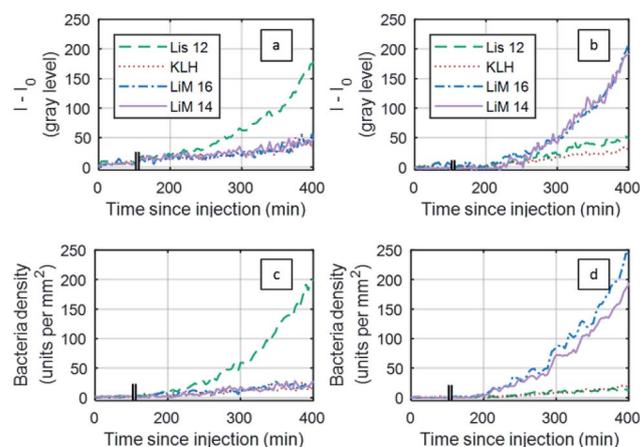

Fig. 5 Experimental results for the detection of *Listeria innocua* (a and c) and *Listeria monocytogenes* (b and d) RO-SPRI: (a and b) SPRI sensorgrams: (c and d) fluid injected at $C_0 = 3 \times 10^4$ CFU mL^{-1} $\pm 10\%$.

Table 1 "Time to onset of positive detection" (in minutes) for two species of *Listeria* at different injection concentrations

Initial concentration (CFU mL^{-1})	Strain	Number of experiments	Time to onset of positive detection (in min)					
			SPRI sensorgrams			Event counting using RO-SPRI		
			Lis12	LiM16	LiM14	Lis12	LiM16	LiM14
2×10^2	*L. monocytogenes*	$n = 2$	—	518 ± 2	528 ± 6	—	432 ± 15	440 ± 17
3×10^4	*L. monocytogenes*	$n = 2$	—	306 ± 6	306 ± 6	—	236 ± 6	236 ± 6
3×10^4	*L. innocua*	$n = 2$	312 ± 8	—	—	246 ± 9	—	—
3×10^4	*L. monocytogenes* & *L. innocua*	$n = 1$	318	316	312	247	247	243

The event detection data calculated from the DIC differential images of bacterial density over time were fitted to a two-parameter model $(t) = A \exp(t/\tau)t$, where $A = C_0 Sv$ and the doubling time $\tau_2 = \tau \ln 2$ (Fig. 4a). As a control or bacterial viability and growth in each experiment, model parameters were estimated for an initial injection rate of 2×10^2 CFU mL^{-1} ($\pm 10\%$), yielding a doubling time of 40.5 ± 2.7 min. This values are in line with what is reported in the literature for growth in optimal conditions.[56] No difference in growth efficiency was seen between the antibody spots. This analysis shows that our fluidic chamber enables close to optimal growth conditions for the bacteria of interest. The residuals of the modelling process, defined as the difference between the model and the experimental data, are available in the ESI.† Considering this doubling time, it is assessed the concentration in solution, 400 min after injection, has doubled ten fold since injection.

The same analysis was also performed on SPRI images (Fig. 4b), leading to a doubling time of 46.7 ± 1.8 min. This difference with the DIC-based analysis can be attributed to the limitation of the SPRI system to differentiate between individual events that are closer than the spatial resolution of the system, leading to an apparent lower increase in the number of bacteria.

3.3 Early detection of bacteria

The objective of the experiments was to detect bacterial presence as soon as possible, quantified by the "onset of positive detection" defined as the time at which the signal-to-noise ratio (SNR) exceeds 3. The noise floor for SNR calculation was estimated from the KLH negative control.

Both SPRI sensorgrams-based analysis and RO-SPRI-based event counting analysis were carried out for the detection of two species of *Listeria*: *L. monocytogenes* and *L. innocua*. The two species were first detected separately at different concentrations. A third type of experiment consisted in the simultaneous detection of both species *L. monocytogenes* and *L. innocua* injected at a concentration of $C_0 = 2 \times 10^4$ CFU mL^{-1} ($\pm 10\%$).

A comparison between the SPRI sensorgram-based analysis and the RO-SPRI-based event counting is presented in Fig. 5 for the detection of *L. monocytogenes* and *L. innocua* injected at $C_0 = 3 \times 10^4$ CFU mL^{-1} ($\pm 10\%$) (Fig. 5). For SPRI sensorgrams, results are generally presented in terms of reflectivity variations: with the imaging components in our apparatus, an intensity variation of 100 grey levels ($I - I_0 = 100$) corresponded to a reflectivity variation of $\sim 1\%$ ($\Delta\%R \sim 1\%$).

In the SPRI sensorgram-based analysis (Fig. 5a), the negative control areas (KLH) showed a drift of 20% between 200 min and 400 min following injection, while in the RO-SPRI-based event counting analysis, the same negative control area (KLH) showed a non-specific signal of less than 13% over the same interval. This difference in the negative control is due to the different processing strategies: in SPRI sensorgrams, intensity changes inside a region of interest also depend on refractive index changes in the fluid medium close to the surface (change of composition due to the consumption of nutrients by the bacteria, light source intensity and/or variations, *etc.*). For RO-SPRI-based event detection, even if the background signal varies, the individual bacterial event counting is unaffected.

In the case of RO-SPRI-based event counting, the "time to onset of positive detection" (SNR > 3) corresponded to a surface density of between 10 and 20 bacteria per mm^2 (between 3 and 6 units per antibody spot), for an average value of 15 ± 4 bacteria per mm^2.

Results of "time to onset of positive detection" estimations for both types of analyses are presented in Table 1. For SPRI sensorgrams, calculated onsets of positive detection, at ~ 9 h for an initial concentration of 2.0×10^2 CFU mL^{-1} and ~ 5 h for an initial injection at 3×10^4 CFU mL^{-1}, are consistent with the literature.[32,57–59] From RO-SPRI data, the surface density at these times of onset of positive detection on SPRI sensorgrams are respectively estimated at 62 ± 10 bacteria per mm^2, and 75 ± 20 bacteria per mm^2.

For RO-SPRI-based event counting, the time to onset of positive detection were reduced by at least 66 min and up to 86 min compared to the sensorgram method. This gain is coherent with the difference between the surface densities at the onset of positive detection of both methods.

4 Conclusion

In this work, we demonstrated a label-free, real-time biosensor using a prism-based, resolution-optimized SPRI system, optimized for the detection of individual bacteria over a relatively wide field of view. This innovative apparatus can detect individual bacteria in a field of view of 1.5 mm^2, a surface area wide enough to image several antibody-functionalized spots, enabling parallel measurement of different bacteria–antibody interactions. By coupling the system to a DIC microscope, we

validated the viability of the fluidic chamber bacterial growth conditions.

The system proved to be effective for the detection of two different species of *Listeria*, both separately and simultaneously. The data analysis showed a gain of at least one hour compared to classical SPRI analysis based on sensorgrams, with an even higher gain of 1 h 30 min for low concentration injection of 2.0×10^2 ($\pm$10%) CFU mL^{-1}. The improvement in the times to onset of positive detection between the two SPRI methods is clear. Indeed, the presence at the surface of even a very small number of bacteria creates a measurable RO-SPRI signal that is not differentiable from noise in SPRI sensorgrams. The ability of our system to detect the presence of bacteria at surface densities as low as 15 ± 4 bacteria per mm^2 is very promising for early detection of bacteria.

To develop further our technique, experiments on complex samples closer to real life applications, such as food matrices, and for the detection of low concentration pathogens, should be perform. Such experiments were already successfully carried out on standard SPRI devices[19] and look therefore like a realistic perspective.

Conflicts of interest

There are no conflicts to declare.

Acknowledgements

Notes and references

1 E. De Boer and R. R. Beumer, *Int. J. Food Microbiol.*, 1999, **50**, 119–130.

2 M. D. Kirk, I. Mckay, G. V. Hall, C. B. Dalton, R. Stafford, L. Unicomb and J. Gregory, *Clin. Infect. Dis.*, 2008, **47**, 392–400.

3 E. Scallan, R. M. Hoekstra, F. J. Angulo, R. V. Tauxe, M. Widdowson, S. L. Roy, J. L. Jones and P. M. Griffin, *Emerging Infect. Dis.*, 2011, **17**, 1–21.

4 *Risk assessment of Listeria monocytogenes in ready-to-eat foods*, WHO/FAO, 2004.

5 S. Jadhav, M. Bhave and E. A. Palombo, *J. Microbiol. Methods*, 2012, **88**, 327–341.

6 B. Mandracchia, J. Palpacuer, F. Nazzaro, V. Bianco, R. Rega, P. Ferraro and S. Grilli, *IEEE J. Sel. Top. Quantum Electron.*, 2019, **25**, 1–6.

7 D. Rodriguez-Lazaro, P. Gonzalez-García, A. Gattuso, M. V. Gianfranceschi and M. Hernandez, *Int. J. Food Microbiol.*, 2014, **184**, 98–105.

8 R. Radhakrishnan and P. Poltronieri, *Biosensors*, 2017, **7**, 1–12.

9 V. Velusamy, K. Arshak, O. Korostynska, K. Oliwa and C. Adley, *Biotechnol. Adv.*, 2010, **28**, 232–254.

10 E. Howe and G. Harding, *Biosens. Bioelectron.*, 2000, **15**, 641–649.

11 J. Suehiro, A. Ohtsubo, T. Hatano and M. Hara, *Sens. Actuators, B*, 2006, **119**, 319–326.

12 L. Yang, Y. Li and G. F. Erf, *Anal. Chem.*, 2004, **76**, 1107–1113.

13 S. M. Chiriacò, I. Parlangeli, F. Sirsi, P. Poltronieri and E. Primiceri, *Electronics*, 2018, **7**, 347.

14 I.-S. Park, W.-Y. Kim and N. Kim, *Biosens. Bioelectron.*, 2000, **15**, 167–172.

15 Z. Shen, M. Huang, C. Xiao, Y. Zhang, X. Zeng and P. G. Wang, *Anal. Chem.*, 2007, **79**, 2312–2319.

16 A. D. Taylor, J. Ladd, Q. Yu, S. Chen, J. Homola and S. Jiang, *Biosens. Bioelectron.*, 2006, **22**, 752–758.

17 Ö. Torun, İ. Hakkı Boyacı, E. Temür and U. Tamer, *Biosens. Bioelectron.*, 2012, **37**, 53–60.

18 O. Lazcka, F. J. D. Campo and F. X. Muñoz, *Biosens. Bioelectron.*, 2007, **22**, 1205–1217.

19 S. Bouguelia, Y. Roupioz, S. Slimani, L. Mondani, M. G. Casabona, C. Durmort, T. Vernet, R. Calemczuk and T. Livache, *Lab Chip*, 2013, **13**, 4024.

20 D. A. Boehm, P. A. Gottlieb and S. Z. Hua, *Sens. Actuators, B*, 2007, **126**, 508–514.

21 M. Varshney, Y. Li, B. Srinivasan and S. Tung, *Sens. Actuators, B*, 2007, **128**, 99–107.

22 D. Puchberger-Enengl, S. Podszun, H. Heinz, C. Hermann, P. Vulto and G. A. Urban, *Biomicrofluidics*, 2011, **5**, 044111.

23 F. Cimaglia, E. De Lorenzis, V. Mezzolla, F. Rossi and P. Poltronieri, *IEEE Sens. J.*, 2016, **16**, 7045–7052.

24 V. Templier, A. Roux, Y. Roupioz and T. Livache, *TrAC, Trends Anal. Chem.*, 2016, **79**, 71–79.

25 Y. Jung, J. Young Jeong and B. Hyun Chung, *Analyst*, 2008, **133**, 697–701.

26 A. K. Trilling, J. Beekwilder and H. Zuilhof, *Analyst*, 2013, **138**, 1619–1627.

27 B. Byrne, E. Stack, N. Gilmartin and R. O'Kennedy, *Sensors*, 2009, **9**, 4407–4445.

28 J. B. Fasoli and R. M. Corn, *Langmuir*, 2015, **31**, 9527–9536.

29 C.-J. Huang, J. Dostalek, A. Sessitsch and W. Knoll, *Anal. Chem.*, 2011, **83**, 674–677.

30 Y. Wang, W. Knoll and J. Dostalek, *Anal. Chem.*, 2012, **84**, 8345–8350.

31 H. J. Lee, A. W. Wark and R. M. Corn, *Langmuir*, 2006, **22**, 5241–5250.

32 A. Morlay, A. Duquenoy, F. Piat, R. Calemczuk, T. Mercey, T. Livache and Y. Roupioz, *Measurement*, 2017, **98**, 305–310.

33 J. A. Hudson, R. J. Lake, M. G. Savill, P. Scholes and R. E. McCormick, *J. Appl. Microbiol.*, 2001, **90**, 614–621.

34 G. Marusov, A. Sweatt, K. Pietrosimone, D. Benson, S. J. Geary, L. K. Silbart, S. Challa, J. Lagoy, D. A. Lawrence and M. A. Lynes, *Environ. Sci. Technol.*, 2012, **46**, 348–359.

35 V. Chabot, C. M. Cuerrier, E. Escher, V. Aimez, M. Grandbois and P. G. Charette, *Biosens. Bioelectron.*, 2009, **24**, 1667–1673.

36 B. Mandracchia, V. Pagliarulo, M. Paturzo and P. Ferraro, *Anal. Chem.*, 2015, **87**, 4124–4128.

37 P. N. Abadian and E. D. Goluch, *Anal. Methods*, 2015, **7**, 115–122.

38 M. Piliarik, L. Párová and J. Homola, *Biosens. Bioelectron.*, 2009, **24**, 1399–1404.

39 F. Bardin, A. Bellemain, G. Roger and M. Canva, *Biosens. Bioelectron.*, 2009, **24**, 2100–2105.

40 L. Laplatine, L. Leroy, R. Calemczuk, D. Baganizi, P. N. Marche, Y. Roupioz and T. Livache, *Opt. Express*, 2014, **22**, 22771–22785.

41 W. W. Baldwin and P. W. Bankston, *Appl. Environ. Microbiol.*, 1988, **54**, 105–109.

42 L. Grosjean, B. Cherif, E. Mercey, A. Roget, Y. Levy, P. N. Marche, M.-B. Villiers and T. Livache, *Anal. Biochem.*, 2005, **347**, 193–200.

43 B. Cherif, A. Roget, C. L. Villiers, R. Calemczuk, V. Leroy, P. N. Marche, T. Livache and M.-B. Villiers, *Clin. Chem.*, 2006, **52**, 255–262.

44 J. B. Fiche, J. Fuchs, A. Buhot, R. Calemczuk and T. Livache, *Anal. Chem.*, 2008, **80**, 1049–1057.

45 E. Mercey, R. Sadir, E. Maillart, A. Roget, F. Baleux, H. Lortat-Jacob and T. Livache, *Anal. Chem.*, 2008, 3476–3482.

46 J. Homola, *Springer Ser. Chem. Sens. Biosens.*, 2006, **4**, 3–44.

47 M. H. Zwietering, J. T. de Koos, B. E. Hasenack, J. C. de Witt and K. van't Riet, *Appl. Environ. Microbiol.*, 1991, **57**, 1094–1101.

48 C. S. Moreira, A. M. N. Lima, H. Neff and C. Thirstrup, *Sens. Actuators, B*, 2008, **134**, 854–862.

49 K. Özdemir and G. Turhan-Sayan, *J. Lightwave Technol.*, 2003, **21**, 805–814.

50 J.-Y. Tinevez, N. Perry, J. Schindelin, G. M. Hoopes, G. D. Reynolds, E. Laplantine, S. Y. Bednarek, S. L. Shorte and K. W. Eliceiri, *Methods*, 2017, **115**, 80–90.

51 W. Hu, G. He, T. Chen, C. Xian Guo, Z. Lu, J. Nimal Selvaraj, Y. Liu and C. Ming Li, *Chem. Commun.*, 2014, **50**, 2133–2135.

52 L. Zhu, Z. Zhao, P. Cheng, Z. He, Z. Cheng, J. Peng, H. Wang, C. Wang, Y. Yang and Z. Hu, *Adv. Mater.*, 2017, **29**, 1700057.

53 Z. Wang, T. Wilkop, D. Xu, Y. Dong, G. Ma and Q. Cheng, *Anal. Bioanal. Chem.*, 2007, **389**, 819–825.

54 E. Ouellet, C. Lausted, T. Lin, C. W. T. Yang, L. Hood and E. T. Lagally, *Lab Chip*, 2010, **10**, 581–588.

55 I. Stojanović, T. J. G. van der Velden, H. W. Mulder, R. B. M. Schasfoort and L. W. M. M. Terstappen, *Anal. Biochem.*, 2015, **485**, 112–118.

56 J.-C. Augustin and V. Carlier, *Int. J. Food Microbiol.*, 2000, **56**, 29–51.

57 V. Nanduri, A. K. Bhunia, S.-I. Tu, G. C. Paoli and J. D. Brewster, *Biosens. Bioelectron.*, 2007, **23**, 248–252.

58 P. Leonard, S. Hearty, J. Quinn and R. O'kennedy, *Biosens. Bioelectron.*, 2004, **19**, 1331–1335.

59 V. Koubová, E. Brynda, L. Karasová, J. Škvor, J. Homola, J. Dostálek, P. Tobiška and J. Rošický, *Sens. Actuators, B*, 2001, **74**, 100–105.